

Numerical simulation of bubble deformation and breakup under simple linear shear flows

Mitsuhiro Ohta^{a,b,*}, Tetsuya Ueta^b, Yozo Toei^c, Edwin Jimenez^d, Mark Sussman^e

^a*Department of Mechanical Science, Graduate School of Technology, Industrial and Social Sciences, Tokushima University, 2-1 Minamijyousanjima-cho, Tokushima 770-8506, Japan*

^b*Department of Mechanical Engineering, Graduate School of Technology, Industrial and Social Sciences, Tokushima University, 2-1 Minamijyousanjima-cho, Tokushima 770-8506, Japan*

^c*High Performance Plastics Company, Sekisui Chemical Co., Ltd., 2-1 Hyakuyama, Mishimagun Shimamoto-cho, Osaka 618-0021, Japan*

^d*Spectral Numerical, LLC, 1942 Broadway St., STE 314C, Boulder, CO 80302, USA*

^e*Department of Mathematics, Florida State University, Tallahassee, FL 32306, USA*

Abstract

Computations for the deformation and breakup of a bubble in liquid, undergoing simple linear shear flow, are compared to the same process for a drop. The coupled level set/volume-of-fluid (CLSVOF) method, on a dynamic adaptive grid, is used to compute the (complex) deformation of the bubble/drop boundary. The numerical results reveal that the shear-induced bubble deformation and breakup process differs significantly from that of the drop system: (1) the magnitude of shear flow necessary for bubble break-up is much larger than that for the drop, and (2) the bubble undergoes unsteady vacillating behavior near the critical “rupture inducing” shear flow region. The differences between the bubble and drop cases are attributed to the differences in the inherent density and viscosity ratios. A “bubble-rupture” morphology map is derived which gives the critical conditions for bubble breakup with respect to the Reynolds and capillary numbers.

Keywords: Bubble deformation, bubble breakup, shear flow, CFD

1. Introduction

The dynamics of the deformation *and breakup* of a drop in immiscible viscous liquids undergoing simple linear shear flow has been investigated extensively due to its fundamental importance in connection with emulsion and materials processing, mixing and reaction devices. The pioneering experimental work of this problem was performed by Taylor [40, 41] in the early 1930s , and the subsequent theoretical and experimental progress up to the 1980s and 1990s was

*Corresponding author: m-ohta@tokushima-u.ac.jp

8 reviewed in Rallison [25] and Stone [33], respectively. By the 2000s, progress in
 9 computational fluid dynamics (CFD) techniques and increased access to power-
 10 ful computing resources led to a surge of research focused on direct simulations
 11 of this problem. In particular, detailed computational investigations of drop
 12 breakup, based on a Volume-of-Fluid (VOF) method (Hirt and Nichols [11])
 13 were presented in Li et al. [22], Renardy and Cristini [29, 31], Renardy et al.
 14 [30], Khismatullin et al. [18], Renardy [26, 27, 28]. Since then, the literature
 15 on computational studies on the deformation and breakup of a single or several
 16 drops in shear flow has continued to grow (Cristini et al. [6], Inamuro et al.
 17 [13], Zhang et al. [45], Bazhlekov et al. [2], Janssen and Anderson [15], Croce
 18 et al. [7], Komrakova et al. [19, 20], Ioannou et al. [14], Hernandez and Rangel
 19 [10], Amani et al. [1], Zhang et al. [48]) and a variety of numerical techniques
 20 have been developed to tackle this problem, including boundary-integral ap-
 21 proaches (Cristini et al. [5], Janssen and Anderson [16]), lattice Boltzmann
 22 methods (Inamuro [12], Komrakova et al. [19]), front tracking schemes (Un-
 23 verdi and Tryggvason [42]), and interface-capturing level set methods (Sussman
 24 et al. [37]). In contrast, few computational studies on bubble deformation *and*
 25 *breakup* can be found. We remark that there has been a number of articles on
 26 the study of lift of *slightly* deformable bubbles (Ervin and Tryggvason [9], Leg-
 27 endre and Magnaudet [21]). We reiterate though, that for bubble deformation
 28 *and breakup* in shear flows, only a few articles exist: (Wei et al. [44], Wang et al.
 29 [43]). In these previous studies, the dynamics (e.g. rotation angle) of bubble
 30 deformation in shear flow was mainly examined. Concerning bubble breakup,
 31 Wei et al. [44] presented only one numerical result for a bubble breakup process
 32 under the condition of Ca (capillary number) = 35. Bubble dynamics in shear
 33 flow, *including breakup*, is of critical importance for a variety of scientific and
 34 engineering processes. We refer the reader to the following experimental studies
 35 relating to bubble deformation in foaming processes, microfluidic devices, and
 36 micro bubbles in the blood circulation system: (Chu et al. [4], Müller-Fischer
 37 et al. [23], Bento et al. [3], Drenckhan and Saint-Jalmes [8]) In particular, it
 38 is the study of bubble deformation as it pertains to high performance plastics
 39 applications which motivates this work. In this article, we present computa-
 40 tional studies of shear-driven deformation *and breakup* of a bubble in insoluble
 41 viscous liquids. Studying bubble break-up via computation rather than exper-
 42 iments simplifies the process of setting a combination of precise simple shear flow
 43 conditions, low Ca conditions, low density ratio, and low viscosity ratios. The
 44 physical properties that distinguish bubble and drop studies are expressed in
 45 terms of the density ratio $\lambda = \rho_b/\rho_m$ and the viscosity ratio $\eta = \mu_b/\mu_m$, where
 46 ρ is the fluid density, μ is the viscosity and the subscripts “b” and “m” denote
 47 the “bubble” or “drop” and the “matrix fluid”, respectively. For a bubble in an
 48 insoluble viscous liquid, $\lambda \simeq 0$ and $\eta \simeq 0$, whereas most studies dealing with a
 49 drop in an immiscible viscous liquid take $\lambda = 1$ and $\eta \simeq 1$.

50 In this work we focus on identifying critical flow states numerically, in terms
 51 of dimensionless quantities, that specify the extreme conditions at which a bub-
 52 ble or drop in shear flow first transitions from deformation to breakup. We
 53 validate our numerical method through comparisons with previous shear-driven

drop and bubble dynamics results and we also examine the effect of drop deformation and breakup sensitivity on domain and grid size. An advantage of studying shear-driven bubble deformation and breakup computationally, rather than experimentally, is that we can easily modify fluid physical properties to ascertain the sensitivity of deformation and breakup to physical parameters. In our computations, the time-evolution of the boundary between gas and liquid is tracked with a coupled level set/volume-of-fluid (CLSOF) interface capturing algorithm (Sussman and Puckett [36], Sussman et al. [38]). We focus on determining critical physical conditions in which the breakup of a bubble occurs in shear flow because it is important to identify the parameter regimes in which a relatively simple system transitions from stable to unstable. Specifically, we identify the critical Reynolds number (Re_c) corresponding to the bubble breakup onset condition as a function of Ca . The critical Reynolds number, Re_c , for drop breakup was reported previously by Li et al. [22]. In previous studies on the motion of bubble deformation in a simple shear flow (Rust and Manga [32], Müller-Fischer et al. [23]), only findings for bubble deformation under very low Re number conditions ($Re \ll 1$) have been reported. In this work we determine, for the first time, the critical Reynolds number ($Re \gg 1$) that leads to *bubble* breakup. Additionally, our computational studies reveal characteristics that distinguish the deformation and breakup processes of a drop versus those of a bubble.

2. Problem Description

Figure 1(a) shows a schematic of the computational system for our studies of a bubble (or drop) in shear flow. The computational domain consists of a three-dimensional rectangular domain of L (length) \times W (width) \times H (height). The size of L , W and H was determined after consideration of numerical result sensitivity to domain size; numerical studies of domain-size dependence are presented in Section 3.3. All computational results that follow were obtained from numerical solutions of the three-dimensional governing equations for gas-liquid/liquid-liquid flows. Computations are initialized with a spherical bubble (or drop) of radius $R = 5$ mm set at the center of the computational domain. The bubble (or drop) is then subjected to a linear shear flow generated by the motion of the top and bottom plates, which have constant velocity $+V$ and $-V$, respectively. In the interior of the domain, the initial velocity condition is assumed to be a simple linear profile and periodic boundary conditions are imposed along the x and y directions. Mathematically, the initial and boundary

90 conditions are described as follows:

$$\phi(x, y, z, 0) = \sqrt{(x - \frac{L}{2})^2 + (y - \frac{W}{2})^2 + (z - \frac{H}{2})^2 - R} \quad (1)$$

$$\mathbf{u}(x, y, z, 0) = \begin{pmatrix} \frac{2V}{H}(z - \frac{H}{2}) \\ 0 \\ 0 \end{pmatrix}$$

$$\phi(x + L, y, z, t) = \phi(x, y, z, t) \quad \phi(x, y + W, z, t) = \phi(x, y, z, t)$$

$$\mathbf{u}(x, y, H, t) = \begin{pmatrix} V \\ 0 \\ 0 \end{pmatrix} \quad \mathbf{u}(x, y, 0, t) = \begin{pmatrix} -V \\ 0 \\ 0 \end{pmatrix}$$

$$\mathbf{u}(x + L, y, z, t) = \mathbf{u}(x, y, z, t) \quad \mathbf{u}(x, y + W, z, t) = \mathbf{u}(x, y, z, t)$$

91 $\phi(x, y, z, t)$ is a material indicator function which is positive in the “matrix”
 92 fluid and negative in the bubble (or drop) fluid. $\mathbf{u}(x, y, z, t)$ is the velocity.

93 Common dimensionless physical parameters used to describe gas-liquid or
 94 liquid-liquid two-phase flows include the Reynolds (Re), Weber (We) (or Ca (=
 95 We/Re)) and Froude (Fr) numbers. Gas-Liquid and Liquid-Liquid two-phase
 96 flow problems are also determined by the density ratio λ and the viscosity ratio
 97 η . In the present study, the effect of gravity is not considered so that we ignore
 98 the effect of the Fr number.

99 When comparing with previous drop studies, we fix $\lambda = 1$. As a result, (for
 100 $\lambda = 1$) the following dimensionless physical parameters are used to describe the
 101 problem of drop deformation/breakup in shear flow

$$Re = \frac{\rho_m U R}{\mu_m}, \quad Ca = \frac{\mu_m U}{\sigma}, \quad \eta = \frac{\mu_b}{\mu_m} \quad m = \text{matrix fluid} \quad (2)$$

102 U is the velocity scale and σ denotes the surface tension. For the problem of
 103 shear-induced drop deformation and breakup, the velocity is set to $U = \Gamma R$,
 104 where the shear-rate is $\Gamma = 2V/H$. As mentioned in the introduction, most
 105 previous drop studies set $\eta = 1$ (e.g. Li et al. [22]). Thus, for comparison
 106 with previous drop deformation and breakup problems, we set $\lambda = \eta = 1$ (and
 107 also neglect the effect of gravity so that $g = 0$). On the other hand, in our
 108 computations for bubble deformation, we set the density and viscosity of air to
 109 be $\rho_b = 1.2 \text{ kg/m}^3$ and $\mu_b = 1.8 \times 10^{-5} \text{ Pa}\cdot\text{s}$ respectively. We emphasize that for
 110 consistency with previous studies (Li et al. [22], Rust and Manga [32], Müller-
 111 Fischer et al. [23], Komrakova et al. [19], Amami et al. [1]), we computationally
 112 examine the deformation and breakup of a bubble in simple linear shear flow
 113 as a function of the Re and Ca numbers. That is to say, by setting $g = 0$,
 114 we are isolating the effect of only varying Re and Ca on bubble deformation
 115 and breakup. In our controlled study, we determine the critical Re_c versus Ca
 116 curve in which Re_c corresponds to the threshold of bubble (or drop) breakup.
 117 We determine the critical Re_c versus Ca curve for strategic pairs of the density
 118 ratio and viscosity ratio.

119 In our computations, the density of the matrix fluid is fixed at $\rho_m = 1000$
 120 kg/m^3 . The surface tension at the bubble (drop) interface is $\sigma = 2.5 \times 10^{-2}$

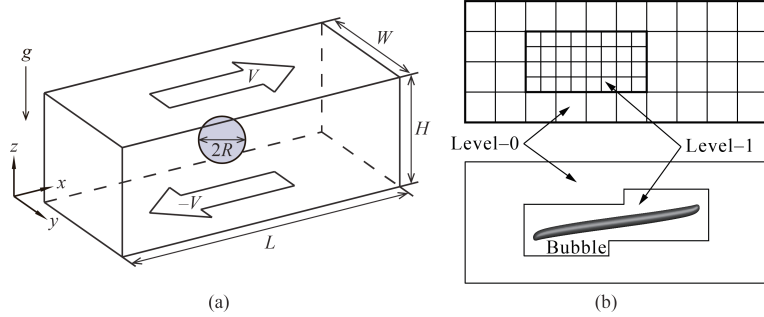


Figure 1: (a) Computational domain schematic for a bubble or drop in shear flow. Gravity is set to zero in our computations in order to isolate the effects of density and viscosity ratios. (b) (upper panel) a two-level adaptive mesh refinement (AMR) grid schematic corresponding to one of our simulations; (lower panel) snapshot of bubble deformation in simple linear shear flow.

121 N/m. The values of Re and Ca in our simulations are controlled by changing
 122 the values of μ_m and V . For studying bubble deformation and break-up, the
 123 density and viscosity ratios satisfy $\lambda = 1.2 \times 10^{-3}$ and $\eta < 1.0 \times 10^{-3}$.

124 3. Numerical Analysis

125 3.1. Numerical method and governing equations

126 Numerical results were obtained using the interface capturing Coupled Level
 127 Set and Volume of Fluid (CLSVOF) method (Sussman and Puckett [36], Suss-
 128 man et al. [38]), which is based on a fixed grid finite volume algorithm. The
 129 CLSVOF method is a robust numerical technique that combines some of the ad-
 130 vantages of the Volume of Fluid (VOF) method (Hirt and Nichols [11]) and the
 131 Level Set (LS) (Sussman et al. [37]) method while overcoming their weaknesses.
 132 In the VOF method, the Volume Fraction function, F , is used to represent
 133 the interface. The values of F correspond to the volume fraction of liquid in
 134 a given computational cell. In other words, $F = 0$ when a computational cell
 135 contains only gas and $F = 1$ when a computational cell contains only liquid.
 136 If $0 < F < 1$, then a computational cell contains the gas-liquid interface. The
 137 VOF method has a great advantage over the LS method in that accurate algo-
 138 rithms for advecting F can be applied so that mass/volume is conserved up to
 139 machine precision while still maintaining a sharp representation of the interface.
 140 On the other hand, the disadvantage of the VOF method in comparison to the
 141 LS method is that tangled and difficult reconstruction procedures are required
 142 for determining the slope of the piecewise linear VOF reconstructed interface.
 143 In the LS method, the signed distance function ϕ (LS function) is used to track
 144 the interface. The interface is implicitly represented by the set of points in which
 145 $\phi = 0$. Liquid and gas regions are defined as $\phi > 0$ in the liquid and $\phi < 0$ in the
 146 gas, respectively. One of the advantages of the LS method is that one can track
 147 and represent smoothly the interface, but the LS method has the disadvantage

148 that mass/volume is not explicitly conserved. In the CLSVOF method, the coupling
 149 between the LS function and the VOF function occurs when computing
 150 the normal of the reconstructed interface in the VOF calculation process and
 151 also when assigning the LS function with the exact signed normal distance to
 152 the reconstructed interface in the LS calculation process. That is to say, the
 153 piecewise linear approximation (the volume-of-fluid reconstruction step) for the
 154 VOF method is determined using the unit normal vector (\mathbf{n}) estimated from
 155 information of the LS function. By taking advantage of both methods, the evo-
 156 lution of the liquid-gas interface location can be computationally captured in
 157 such a way so that volume/mass is preserved to machine precision and at the
 158 same time, the interface normals and the surface tension force (which is pro-
 159 portional to the interface curvature) can be straightforwardly derived from the
 160 smooth level set function.

161 In our studies, the two-phase fluid flow is comprised of air and a viscous
 162 Newtonian liquid. The Heaviside function, $\mathcal{H}(\phi)$, which is defined as

$$\mathcal{H}(\phi) = \begin{cases} 1 & \phi \geq 0 \\ 0 & \phi < 0 \end{cases} \quad (3)$$

will be used below to distinguish each of the two fluids. A single set of three-dimensional equations governs the motion of both fluids, which are taken to be incompressible, and consists of the continuity equation and the Navier-Stokes equations with surface tension forces:

$$\nabla \cdot \mathbf{u} = 0 \quad (4)$$

$$\frac{\partial \mathbf{u}}{\partial t} + (\mathbf{u} \cdot \nabla) \mathbf{u} = \frac{1}{\rho} \nabla \cdot (-p \mathbf{I} + 2\mu \mathbf{D}) + \mathbf{g} - \frac{\sigma \kappa}{\rho} \nabla \mathcal{H} \quad (5)$$

163 where \mathbf{u} is the velocity vector, t represents time, p is the pressure, \mathbf{I} is the unit
 164 tensor, \mathbf{D} is the rate of deformation tensor ($\mathbf{D} = \frac{1}{2}(\nabla \mathbf{u} + (\nabla \mathbf{u})^T)$), ρ is the
 165 density, μ is the viscosity, κ is the interfacial curvature, and the Heaviside func-
 166 tion $\mathcal{H}(\phi)$ is a function of the level set (LS) function ϕ . The singular Heaviside
 167 gradient term in the right hand side of equation (5) is a body force representing
 168 the surface tension force and is equivalent to specifying that the jump in the
 169 normal stress is equal to $\sigma \kappa$ (Tanguy et al. [39]). The surface tension force
 170 expressed by the singular Heaviside gradient term acts only on the gas-liquid
 171 interface. The sharp interface “Ghost Fluid Method” (Kang et al. [17]) is used
 172 to discretize the gradient of the Heaviside function as it appears in the surface
 173 tension force term. This force, upon discretization, is only non-zero across cells
 174 in which the level set function changes sign.

175 The interfacial curvature κ is computed with second order accuracy directly
 176 from the volume-of-fluid (VOF) function using the height function technique
 177 (Sussman [34], Sussman et al. [38]). We remark that we get the same results if
 178 we were to compute κ directly from the LS function using the “level set” height
 179 function technique.

180 Since ρ and μ are taken to be constant in each fluid, with a jump at the
181 interface, they can be expressed in terms of the Heaviside function,

$$\rho = \rho_m \mathcal{H} + \rho_b (1 - \mathcal{H}), \quad \mu = \mu_m \mathcal{H} + \mu_b (1 - \mathcal{H}). \quad (6)$$

The subscripts “b” and “m” refer to “drop or bubble” and “matrix fluid”, respectively. To represent the free surface with the CLSVOF method, we must evolve the solution to both the VOF equation for F and the LS equation for ϕ :

$$\frac{\partial F}{\partial t} + (\mathbf{u} \cdot \nabla) F = 0, \quad \frac{\partial \phi}{\partial t} + (\mathbf{u} \cdot \nabla) \phi = 0. \quad (7)$$

182 In all computations the discretized variables p , ϕ and F are located at cell
183 centers and the discrete variable \mathbf{u} is located at cell face centers. Our com-
184 putations are performed using an overall second-order accurate hydrodynamic
185 scheme. The spatial discretization uses second-order accurate, slope-limited,
186 upwind techniques for the nonlinear advective terms. The velocity and pressure
187 fields are computed using an implicit pressure projection procedure.

188 The temporal discretization of our numerical method is an operator split
189 projection method as described by Sussman et al. [38]. An outline of our method
190 is as follows (see Sussman et al. [38], section 4, for more details):

191 **Timestep Δt** The timestep is governed by the CFL condition and surface ten-
192 sion (section 5.7 of Sussman et al. [38]):

$$\Delta t < \min_{i,j,k} \left(\frac{\Delta x}{2|U^n|}, \frac{1}{2} \sqrt{\frac{\rho^L}{8\pi\sigma}} \Delta x^{3/2} \right)$$

Step 1. CLSVOF interface advection

$$\begin{aligned} \phi^{n+1} &= \phi^n - \Delta t [\mathbf{u} \cdot \nabla \phi]^n \\ F^{n+1} &= F^n - \Delta t [\mathbf{u} \cdot \nabla F]^n \end{aligned}$$

Step 2. Nonlinear advective force terms

$$\mathcal{A} = [\mathbf{u} \cdot \nabla \mathbf{u}]^n$$

Step 3. Viscosity force

$$\frac{\mathbf{u}^* - \mathbf{u}^n}{\Delta t} = -\mathcal{A} + g\vec{z} - [\nabla p / \rho]^n + \frac{1}{2} \frac{\nabla \cdot (2\mu \mathbf{D}^n) + \nabla \cdot (2\mu \mathbf{D}^*)}{\rho}$$

193 **Step 4. Pressure projection and ghost fluid surface tension algorithm**

$$\mathbf{V} = \mathbf{u}^n + \Delta t (-\mathcal{A} + g\vec{z} + \frac{1}{2} \frac{\nabla \cdot (2\mu \mathbf{D}^n) + \nabla \cdot (2\mu \mathbf{D}^*)}{\rho})$$

194

$$\mathbf{V} = \mathbf{V} - \Delta t \frac{\sigma \kappa(\phi^{n+1})}{\rho} \nabla \mathcal{H}(\phi^{n+1})$$

195

$$\nabla \cdot \frac{\nabla p}{\rho} = \frac{1}{\Delta t} \nabla \cdot \mathbf{V}$$

196

$$\mathbf{u}^{n+1} = \mathbf{V} - \Delta t \frac{\nabla p}{\rho}$$

197 To make efficient use of computational resources, our numerical simulations
 198 utilize an adaptive hierarchy of grids based on a dynamic adaptive mesh refine-
 199 ment (AMR) technique (Sussman et al. [35]). Adaptive grids are dynamically
 200 adjusted based on the location of the deforming gas-liquid interface. In the AMR
 201 technique the grid resolution is increased in regions near the interface while a
 202 coarser grid is used where the flow is relatively steady. The upper panel of
 203 Figure 1(b) displays a schematic view of the hierarchical grid structure and the
 204 lower panel corresponds to an actual computational example for bubble defor-
 205 mation in simple linear shear flow. In general, the mesh hierarchy is composed
 206 of different levels of refinement ranging from coarsest $\ell = 0$ (“level-0”) to finest
 207 $\ell = \ell_{\max}$ (“level- ℓ_{\max} ”). The refinement ratio of one grid size ($\Delta x = \Delta y = \Delta z$)
 208 to the next finer level is two so that $\Delta x^{\ell+1} = 0.5\Delta x^\ell$. All computations in
 209 this study used an AMR system with a maximum prescribed level $\ell_{\max} = 1$
 210 (as illustrated in the upper panel of Figure 1(b)). In our adaptive mesh refine-
 211 ment algorithm, the velocity in coarse grid cells that neighbor fine grid cells is
 212 interpolated from the coarse grid using bilinear interpolation in order to ini-
 213 tialize “ghost” fine cells. Thus, the bilinear interpolation procedure produces
 214 interpolated fine grid data as a linear combination of the coarse grid data.

215 3.2. Validation of the numerical method

216 Numerical studies reported in this section are presented in order to verify
 217 the accuracy of our computational method. First, we compare quantitatively
 218 against the steady-state drop deformation results reported by Li et al. [22]. The
 219 shape of a deformed drop in simple linear shear flow is described in terms of the
 220 Taylor deformation parameter $D = (a - b)/(a + b)$, where a and b are the major
 221 and minor axes of the deformed drop. For consistency, we perform numerical
 222 simulations using CLSVOF over the same computational domain and grid size
 223 used in Li et al. [22], which has dimensions $L(8R) \times W(4R) \times H(8R)$ (recall that
 224 R is the bubble/drop radius) and a level-0 grid size $\Delta x = \Delta y = \Delta z = R/8$;
 225 our two-level AMR grid structure also uses a finer level-1 grid size $\Delta x^{\ell=1} =$
 226 $\Delta y^{\ell=1} = \Delta z^{\ell=1} = R/16$. Numerical results are listed in Table 1 for D as a
 227 function of Re , with $Ca = 0.3$ and $\lambda = \eta = 1$ fixed in every case, obtained with
 228 the VOF method used in Li et al. [22], and also with our CLSVOF algorithm.

Table 1: Comparison of the Taylor deformation parameter D for a drop as a function of Re ($Ca = 0.3$, $\lambda = \eta = 1$). In all cases, the domain size is $L(8R) \times W(4R) \times H(8R)$, where R is the drop radius. CLSVOF method computations used a two-level AMR computational domain with a level-0 discretization $\Delta x^{\ell=0} = \Delta y^{\ell=0} = \Delta z^{\ell=0} = R/8$ and a level-1 discretization $\Delta x^{\ell=1} = \Delta y^{\ell=1} = \Delta z^{\ell=1} = R/16$.

| Reynolds number | 0.1 | 0.5 | 0.6 | 0.75 |
|----------------------|--------|--------|--------|---------|
| D (Li et al. [22]) | 0.3968 | 0.45 | 0.4768 | Breakup |
| D (Our study) | 0.3960 | 0.4570 | 0.4758 | Breakup |

229 Table 1 indicates that our numerical results are in good agreement with previous
 230 computations for drop deformation and breakup.

231 Next, we examine the validation of our computational method in which we
 232 compare with the “bubble deformation in simple linear shear flow” results re-
 233 ported by Müller-Fischer et al. [23]. Müller-Fischer et al. [23] experimentally
 234 inquired into the bubble deformation under the condition of $Re \approx 0$. In our
 235 study, we computed the bubble deformation on a computational domain with
 236 dimensions $L(12R) \times W(6R) \times H(6R)$ and a computational grid in which the
 237 finest level grid size was $\Delta x^{\ell=1} = \Delta y^{\ell=1} = \Delta z^{\ell=1} = R/16$. Computations
 238 were performed for the conditions of $Ca = 0.96$ and $Ca = 1.63$ with $Re \approx 0$
 239 ($Re = 5.0 \times 10^{-4}$), $\lambda = 1.2 \times 10^{-3}$ and $\eta \leq 1.2 \times 10^{-6}$. The parameters
 240 that we have prescribed are consistent with the experimental conditions by
 241 Müller-Fischer et al. [23]. Comparisons of our numerical results and previous
 242 experimental results (Müller-Fischer et al. [23]) are tabulated in Table 2. Ad-
 243 ditionally, in Table 2, we also list experimental results with the condition of
 244 $Re \approx 0$ and $\lambda \approx \eta \approx 0$ by Rust and Manga [32]. These experimental values
 245 were obtained from the graph showing the relation of D vs Re (Rust and Manga
 246 [32]). As is clear from Table 2, our numerical results predicted larger values of
 247 D than experimental ones reported by Müller-Fischer et al. [23]. Nevertheless,
 248 we found that our numerical results are very close to the experimental results
 249 by Rust and Manga [32], which emphasizes the intrinsic difficulties associated
 250 with experimental investigations of bubble dynamics, even in simple linear shear
 251 flow. These comparisons suggest that our computational method is effective and
 252 robust at reproducing bubble dynamics in simple linear shear flow.

Table 2: Comparison of D for a bubble as a function of Ca ($Re \approx 0$, $\lambda \approx \eta \approx 0$). In all cases, the domain size is $L(12R) \times W(6R) \times H(6R)$. CLSVOF computations used a two-level AMR computational domain with a level-0 discretization $\Delta x^{\ell=0} = \Delta y^{\ell=0} = \Delta z^{\ell=0} = R/8$ and a level-1 discretization $\Delta x^{\ell=1} = \Delta y^{\ell=1} = \Delta z^{\ell=1} = R/16$.

| Capillary number | 0.96 | 1.63 |
|---|-----------------|-----------------|
| D (Müller-Fischer et al. [23]) | 0.37 | 0.58 |
| D (Rust and Manga [32]) | 0.71 ± 0.05 | 0.81 ± 0.02 |
| D (Our study $\Delta x^{\ell=1} = R/16$) | 0.63 | 0.75 |

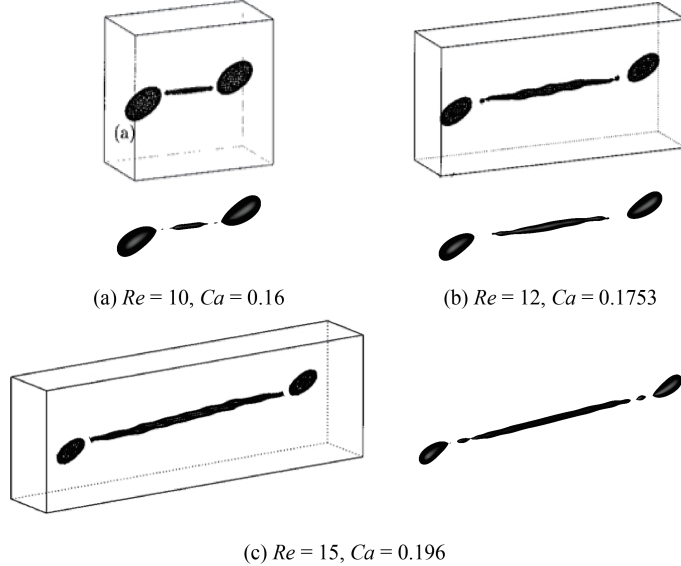


Figure 2: Comparison with results reported in Renardy and Cristini [31] (shown in boxes) for drop breakup in shear flow. In Renardy and Cristini [31], the computational domain dimensions were $W = 4R$, $H = 8R$, and L was varied depending on the Re and Ca conditions. The grid size in Renardy and Cristini [31] was set to $\Delta x = \Delta y = \Delta z = R/8$. Reprinted with permission from reference Renardy and Cristini [31]. Copyright 2001, AIP Publishing. Results obtained with our CLSVOF algorithm, corresponding to each case in reference Renardy and Cristini [31], are shown outside boxes. The CLSVOF method used a two-level AMR computational domain with a level-0 discretization $\Delta x^{\ell=0} = \Delta y^{\ell=0} = \Delta z^{\ell=0} = R/8$ and a level-1 discretization $\Delta x^{\ell=1} = \Delta y^{\ell=1} = \Delta z^{\ell=1} = R/16$. The onset of drop breakup is demonstrated for (a) $Re = 10$, $Ca = 0.16$, (b) $Re = 12$, $Ca = 0.1753$, and (c) $Re = 15$, $Ca = 0.196$. For all three Re and Ca conditions, $\lambda = \eta = 1$.

Finally, we present a comparison with numerical results for drop breakup reported in Renardy and Cristini [31]. Figure 2 demonstrates drop breakup with pinch-off behavior for three Re and Ca conditions and with constant values of $\lambda = \eta = 1$ for all cases. The three cases that we consider correspond to (a) $Re = 10$, $Ca = 0.16$, (b) $Re = 12$, $Ca = 0.1753$, and (c) $Re = 15$, $Ca = 0.196$, and which are illustrated in Figures 2(a)-(c), respectively. The results reported in Renardy and Cristini [31], which were obtained with a VOF method, are shown inside boxes while results obtained with our CLSVOF approach are displayed outside boxes. In the computations presented in Renardy and Cristini [31], the dimensions $W = 4R$ and $H = 8R$ were fixed, while L was changed depending on Re and Ca conditions, and the grid size was set to $\Delta x = \Delta y = \Delta z = R/8$. To compare with their results, we performed simulations with the CLSVOF method over a two-level AMR computational domain of the same dimensions and the same level-0 discretization: $\Delta x^{\ell=0} = \Delta y^{\ell=0} = \Delta z^{\ell=0} = R/8$; we set the finer level-1 grid size $\Delta x^{\ell=1} = \Delta y^{\ell=1} = \Delta z^{\ell=1} = R/16$. The results shown in Figure 2 verify that our numerical approach can reproduce

269 the same drop breakup behavior presented in Renardy and Cristini [31]. Slight
 270 differences between the results can be attributed to the increased resolution used
 271 in our study in the level-1 grid around the elongated drop.

272 The numerical validation studies performed in this section and the follow-
 273 ing section demonstrate that our numerical method can reliably determine the
 274 transition regions at which shear-induced bubble or drop deformation leads to
 275 breakup. We remark that in the next section, we demonstrate that we can
 276 expect an error of 3% for predicting the transition to break-up. The analysis
 277 in this section and the following also demonstrate that the error is reduced by
 278 a factor of 2 each time the grid is refined by a factor of 2. Also, we refer the
 279 reader to Ohta et al. [24] in which we apply our CLSVOF method for bubble
 280 formation problems.

281 *3.3. Consideration of domain and grid sizes*

282 *3.3.1. Selecting the appropriate domain size*

283 The computational domain size used in numerical studies can affect the
 284 behavior of drop deformation and breakup. Referring to Figure 1(a), with an
 285 appropriately large domain length L and a fixed width $W = 4R$, the effect of
 286 the height H on drop behavior was examined in Li et al. [22] for Stokes flows
 287 and various Ca conditions and in Komrakova et al. [19] for $Re = 1$ and $Ca =$
 288 0.27. Other related studies investigated drop breakup sensitivity (Renardy and
 289 Cristini [29]) and drop deformation sensitivity (Renardy et al. [30]) with respect
 to the entire domain size.

Table 3: Comparison of the Taylor deformation parameter D for a drop as a function of domain size ($Re = 0.75$, $Ca = 0.3$, $\lambda = \eta = 1$). CLSVOF method computations used a two-level AMR computational domain with a level-0 discretization $\Delta x^{\ell=0} = \Delta y^{\ell=0} = \Delta z^{\ell=0} = R/8$ and a level-1 discretization $\Delta x^{\ell=1} = \Delta y^{\ell=1} = \Delta z^{\ell=1} = R/16$.

| System | Domain size ($L \times W \times H$) | D |
|----------|---------------------------------------|---------|
| System 1 | $8R \times 4R \times 8R$ | Breakup |
| System 2 | $12R \times 4R \times 8R$ | Breakup |
| System 3 | $8R \times 4R \times 6R$ | 0.541 |
| System 4 | $8R \times 6R \times 6R$ | 0.466 |
| System 5 | $8R \times 8R \times 8R$ | 0.460 |
| System 6 | $8R \times 16R \times 16R$ | 0.460 |

290
 291 Here we investigate the drop dynamics sensitivity to domain size around
 292 the critical Reynolds number $Re_c = 0.75$. Specifically, we consider domain size
 293 sensitivity for the condition of $Re = 0.75$, $Ca = 0.3$, and $\lambda = \eta = 1$, which is a
 294 condition used in the comparison studies of the previous section. As shown in
 295 Table 1, the drop breaks up for the condition of $Re = 0.75$ and $Ca = 0.3$ with
 296 a domain size of $L(8R) \times W(4R) \times H(8R)$. Results for domain size sensitivity
 297 for six domain systems, all of which use a level-1 grid size $\Delta x^{\ell=1} = \Delta y^{\ell=1} =$
 298 $\Delta z^{\ell=1} = R/16$, are tabulated in Table 3. Note that the domain size used in the
 299 comparison study (Table 1) corresponds to System 1.

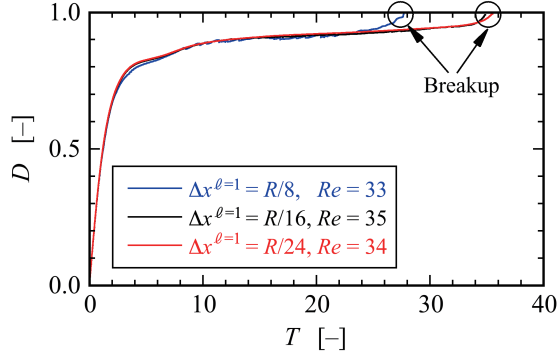


Figure 3: Time evolution of the deformation parameter D versus dimensionless time $T = \Gamma t$ for a bubble, obtained with three grid systems at different resolutions. All three resolutions use a two-level AMR grid with an effective fine resolution grid size $\Delta x^{\ell=1} = \Delta y^{\ell=1} = \Delta z^{\ell=1}$. The evolution of D using the first system, where $\Delta x^{\ell=1} = R/8$, is shown in blue and it predicts that bubble breakup occurs at a Reynolds number $Re = 33$. The evolution of D using the second system, where $\Delta x^{\ell=1} = R/16$, is shown in black and it predicts that bubble breakup occurs at a Reynolds number $Re = 35$. Results with the third system, shown in red, use $\Delta x^{\ell=1} = R/24$, and they predict that breakup occurs at $Re = 34$. The capillary number corresponding to these results is $Ca = 1.0$. ($\lambda = 1.2 \times 10^{-3}$, $\eta < 1.0 \times 10^{-3}$)

300 The results in Table 3 suggest that drop deformation is promoted when we
 301 use a domain size with $W = 4R$. In contrast, the drop does not break up and
 302 becomes stable with a deformed shape if we set L large enough and $W \geq 6R$ and
 303 $H \geq 6R$. Since the value of D for the domain size $L(8R) \times W(6R) \times H(6R)$ differs
 304 by only 1.3% with the value for the domain size of $L(8R) \times W(16R) \times H(16R)$,
 305 in the results that follow we set the width to $W = 6R$ and the height to $H = 6R$
 306 to minimize the number of computational grid nodes along those directions. To
 307 determine the critical Reynolds number Re_c (with $Ca = 0.3$), we consider a
 308 domain size of $L(24R) \times W(6R) \times H(6R)$, and we find that the drop reaches a
 309 stable state with deformation parameter $D=0.549$ for $Re = 1.0$, while a value
 310 of $Re = 1.1$ leads to drop breakup.

311 *3.3.2. Selecting the appropriate grid size*

312 The grid size and adaptive meshing strategy that we adopt is chosen in order
 313 to answer the research question as to the conditions which determine whether
 314 a bubble in shear flow will break-up or not. In such a case, we must accurately
 315 capture the balance of forces with respect to the (non-local) force exerted from
 316 the wall driven flow acting against the interfacial surface tension force. The
 317 accuracy of the “Critical Reynolds Number” depends on the largest Taylor De-
 318 formation parameter D that is supported by the grid (see e.g. Figures 8 and
 319 11). As we report here, we have found that as long as the grid size is fine enough
 320 to support a Taylor Deformation parameter $D < 0.95$, then the transition re-
 321 gion (i.e. “Critical Reynolds number”) (see Figures 3 and 12) will be captured
 322 with a tolerance of three percent. The simulation time becomes impractical if

323 we were to try to further improve the “critical Reynolds number” accuracy. A
324 smaller tolerance would necessitate a larger supported Deformation parameter
325 D which would in turn necessitate a higher aspect ratio computational domain,
326 increased droplet surface area at break-up, increased number of time steps, and
327 higher resolution for representing the drop/bubble at its thinnest point.

328 We make the distinction between our present research, and the research
329 found in the work of Zhang et al. [46, 47] on predicting the conditions for bubble
330 mergers. Even in the most extreme cases for mergers, the largest Deformation
331 parameter never exceeds 0.4 in Zhang et al. [46]. In summary, our gridding
332 requirements necessitate grid points distributed relatively evenly throughout the
333 computational domain when a bubble is stretched to a $D = 0.9$ Deformation,
334 whereas in Zhang et al. [46] the gridding strategy necessitates a more localized
335 strategy.

336 The numerical results presented in this and the previous section used a
337 finest-level grid size set to $\Delta x^{\ell=1} (= \Delta y^{\ell=1} = \Delta z^{\ell=1}) = R/16$. To verify the
338 adequacy of this grid resolution, we present rid refinement results for a bubble
339 breakup simulation with $Ca = 1.0$, which corresponds to the most deformable
340 and stretchable bubble case considered in our numerical studies. We use three
341 different grid systems, (i) $\Delta x^{\ell=1} = R/8$, (ii) $\Delta x^{\ell=1} = R/16$, and (iii) $\Delta x^{\ell=1} =$
342 $R/24$, in order to determine Re_c . Figure 3 shows the time evolution of the
343 deformation parameter D over time for the three grid systems; the x -axis is a
344 dimensionless time defined by $T = It$ and the y -axis is D . The results show that
345 bubble breakup occurs at $Re_c = 35$ for the grid system with $\Delta x^{\ell=1} = R/16$,
346 while the finer computational grid with $\Delta x^{\ell=1} = R/24$ predicts a critical value of
347 $Re_c = 34$. For the $\Delta x^{\ell=1} = R/8$ results, it is clear that the $R/8$ resolution is too
348 coarse in order to capture the proper break-up time, albeit the critical Reynolds'
349 number, $Re_c = 33$, was still close to the finer grid resolution cases. Note that
350 although the time evolution of D for the two finer resolution systems ($R/16$ and
351 $R/24$) is consistent between the two, (the predicted critical Reynolds numbers
352 differ by $\sim 3\%$), the computational time using the grid system with $\Delta x^{\ell=1} =$
353 $R/24$ was more than 6 times longer than the one based on the coarser system
354 with $\Delta x^{\ell=1} = R/16$. We remark that in our search for Re_c , we considered a wide
355 range of values of Ca and we found it necessary to use a large L ($\sim 24R$) since
356 for certain shear flows the bubble can stretch significantly without breaking up.
357 Nevertheless, for the conditions presented in this section, the results indicate
358 that our numerical approach, even with a finest-level resolution set to $\Delta x^{\ell=1} =$
359 $R/16$, is capable of accurately reproducing bubble deformation and breakup
360 without sacrificing any essential dynamical features.

361 **4. Results and Discussion**

362 *4.1. Drop deformation and breakup*

363 To illustrate the differences in deformation and breakup between a drop
364 and a bubble around critical conditions, we first present numerical results for
365 drop deformation. The time evolution of drop deformation and breakup in

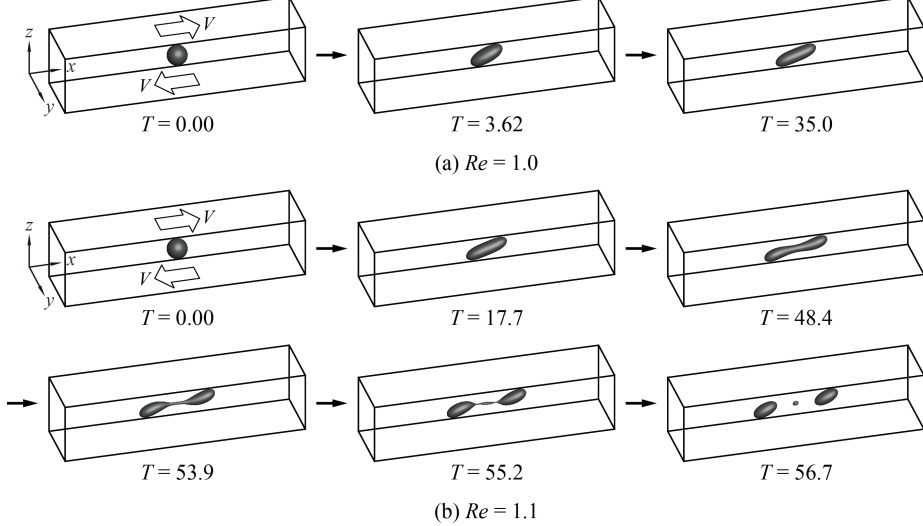


Figure 4: Time evolution of drop deformation and breakup in shear flow at the condition of $Ca = 0.3$ with (a) $Re = 1.0$ and (b) $Re = 1.1$. The “drop” critical Reynolds number corresponding to $Ca = 0.3$ is $1.0 < Re_c < 1.1$. ($\lambda = \eta = 1.0$)

simple linear shear flow for two conditions is shown in Figure 4; the first case, shown in Figure 4(a), uses $Ca = 0.3$ and $Re = 1.0$, while the second case, depicted in Figure 4(b), uses $Ca = 0.3$ and $Re = 1.1$. Using a domain size of $L(24R) \times W(6R) \times H(6R)$, in the case with $Re = 1.0$, the drop gradually deforms and finally attains a stable deformed state with $D = 0.549$. Over the same domain, for the case with $Re = 1.1$, the “mother” drop elongates over time and the volume at the ends of the deforming drop expands; that is, both ends of the drop become bulb-shaped. As time progresses, particularly over the time interval $48.4 \leq T \leq 55.2$, a thread-bridge forms between the bulbous ends and the thread-bridge becomes thinner. Finally, at around the dimensionless time $T \sim 56.7$, the mother drop breaks up, forming two “daughter” drops through the pinch off; one satellite drop is also generated between the pinched off daughter drops.

4.2. Bubble deformation and breakup

Next we present numerical results that illustrate the conditions that lead to bubble deformation without breakup as well as conditions where the bubble deforms and ultimately breaks up. The time evolution of shear-induced bubble deformation without breakup at the condition of $Ca = 0.3$ and $Re = 92$ is depicted in Figure 5 and the bubble breakup process with flow condition of $Ca = 0.3$ and $Re = 93$ is illustrated in Figure 6. The results indicate that the critical Reynolds number is approximately $Re_c = 93$ (with $Ca = 0.3$). A comparison with the drop breakup dynamics presented in Section 4.1 and the corresponding processes for bubble deformation and breakup exhibit very

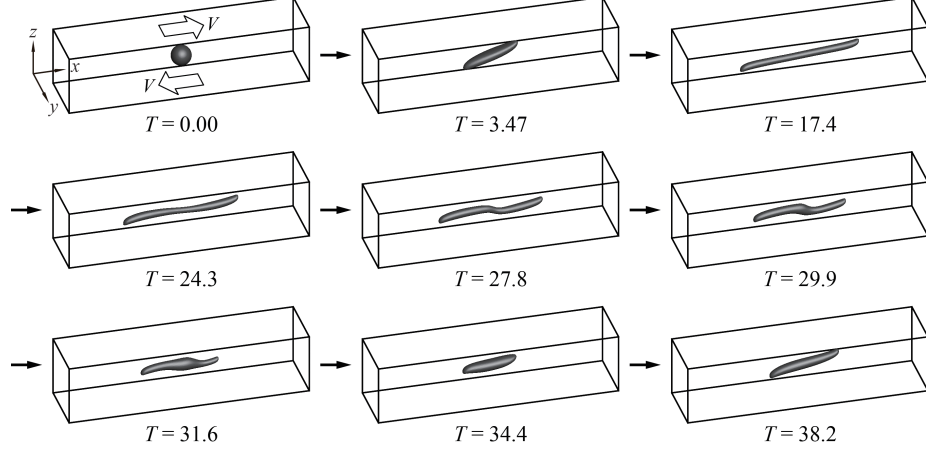


Figure 5: Time evolution of bubble deformation in shear flow at the condition of $Ca = 0.3$ and $Re = 92$. The “bubble” critical Reynolds number corresponding to $Ca = 0.3$ is $92 < Re_c < 93$. In contrast to the drop deformation case, when Re is slightly below Re_c (See Figure 4 $Re = 1.0$ for the drop case), the bubble shape will not reach a steady shape, instead the bubble shape alternates between the shapes “slightly stretched” ($T = 3.47$), fully stretched and “doglegged” ($T = 27.8$) and “almost” back to the original “slightly stretched” case ($T = 34.4$). ($\lambda = 1.2 \times 10^{-3}$, $\eta < 1.0 \times 10^{-3}$)

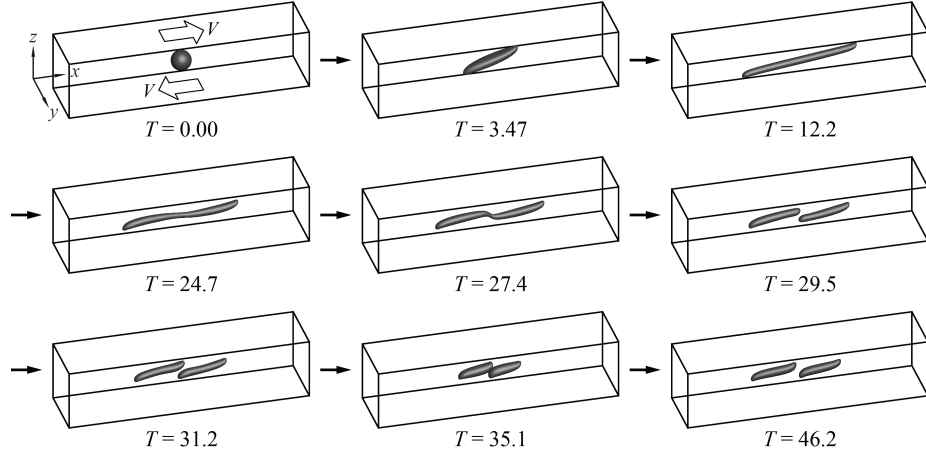


Figure 6: Time evolution of bubble deformation in shear flow at the condition of $Ca = 0.3$ and $Re = 93$. The “bubble” critical Reynolds number corresponding to $Ca = 0.3$ is $92 < Re_c < 93$. ($\lambda = 1.2 \times 10^{-3}$, $\eta < 1.0 \times 10^{-3}$)

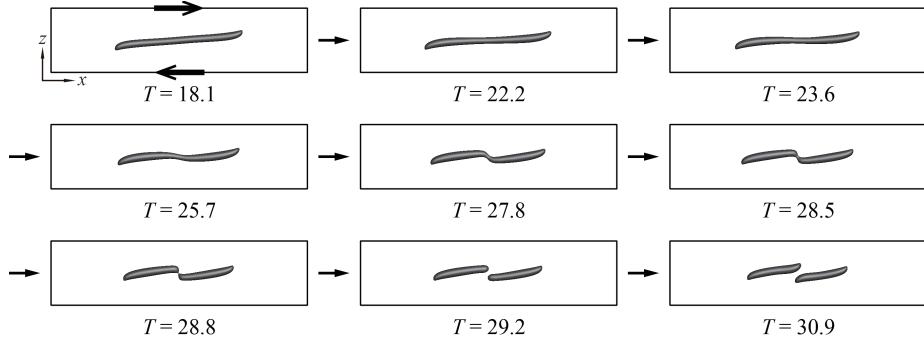


Figure 7: Detail of bubble breakup process in shear flow at the condition of $Ca = 0.3$ and $Re = 93$. The “bubble” critical Reynolds number corresponding to $Ca = 0.3$ is $92 < Re_c < 93$. ($\lambda = 1.2 \times 10^{-3}$, $\eta < 1.0 \times 10^{-3}$)

389 distinct features. First, we note that a relatively large shear force magnitude is
 390 required for bubble breakup ($\lambda = 1.2 \times 10^{-3}$, $\eta < 1.0 \times 10^{-3}$) compared with the
 391 case of the drop ($\lambda = \eta = 1$). Then, for the same value of $Ca = 0.3$, the critical
 392 Reynolds number for the bubble is around 85 times larger than that for the
 393 drop. Focusing on the bubble dynamics with no-breakup (Figure 5), the results
 394 show that the bubble is largely elongated in the x -direction at the early stages
 395 ($T \leq 24.3$) of bubble deformation, but the bubble does not develop the bulb-
 396 like shape (large volume areas) at both ends present in the drop deformation
 397 process. It is also evident that the ends of the deforming bubble develop cusped
 398 shapes under the influence of the strong shear flow. A noteworthy feature for
 399 the non-breaking bubble is that it does not settle into a deformed stable state
 400 as in the case of drop deformation presented in Figure 4(a). After an initial
 401 elongation process, the bubble enters a shrinking phase ($T = 27.8$) where the
 402 doglegged shape formed at the center of the bubble returns to a smaller deformed
 403 shape ($T = 34.4$) that is similar to its earlier shape ($T = 3.47$). However, when
 404 we compare the early deformed bubble shape at $T = 3.47$ with the shape at
 405 $T = 34.4$, it is clear that the shapes are not identical. Following the shrinking
 406 phase, the bubble begins to stretch again ($T = 38.2$) and the bubble oscillates
 407 between its elongated shape and shortened geometry.

408 For the case of bubble breakup (Figure 6), we observe that the deformation
 409 process is almost the same as the no-breakup case until the doglegged shape
 410 is formed at $T \sim 27.4$. The bubble finally breaks during the time interval
 411 $27.7 \leq T \leq 29.5$. For a closer examination of the bubble breakup process,
 412 a detailed panel of cross-sectional slices in the xz -plane through the bubble
 413 shape center is presented in Figure 7. The images displayed in Figure 7, which
 414 are taken at shorter time intervals than those shown in Fig. 6, reveal that the
 415 bubble breaks up into two daughter bubbles due to the pinch off at the thread-
 416 bridge part of the doglegged shape during the shrinking process ($T = 28.5 \sim$
 417 28.8). After breaking up, the two daughter bubbles migrate to the center: the
 418 left daughter bubble moves toward the right-side of the domain and the right

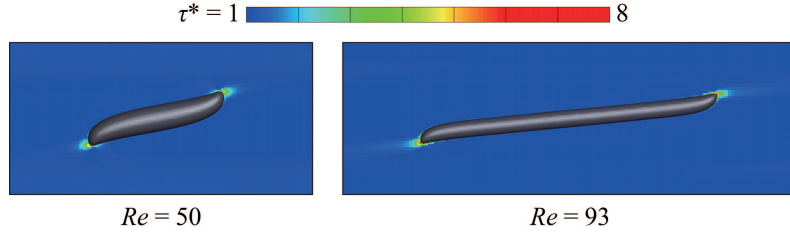


Figure 8: Normalized shear stress τ^* around a bubble for two Reynolds numbers under the condition of $Ca = 0.3$. The left image shows the shear stress profile at $Re = 50$ and the right image at $Re = 93$.

daughter bubble moves to the left side (see results for $T = 29.5 \sim 35.1$ in Figure 6 and for $T = 28.8 \sim 30.9$ in Figure 7). The two daughter bubbles then momentarily congregate near the domain center ($T = 35.1$ in Figure 6), before they slowly start to separate: the left daughter bubble moves to the left and the right daughter bubble moves to the right ($T = 46.2$ in Figure 6). The results clearly demonstrate that the bubble breakup process is markedly different from the analogous drop breakup process.

4.3. Shear stress acting on the bubble

In the previous section, the appearance of bubble deformation and breakup was discussed. It is expected that a large deformation and breakup of the bubble are closely related to the state of shear stress acting on the bubble. Figure 8 shows the shear stress profile around a bubble for two Reynolds numbers under the condition of $Ca = 0.3$: Reynolds number equal to 50 and 93. The shear stress profile on the left corresponds to the case of $Re = 50$ and the right side shows the shear stress profile for the case of $Re = 93$. The normalized shear stress, $\tau^* = \tau/\tau_0$, is defined as a ratio of the local shear stress $\tau = \mu_m \sqrt{2\mathbf{D} : \mathbf{D}}$ and the apparent shear stress $\tau_0 = \mu_m \Gamma$. In this study, for a given Ca condition, the same value of τ_0 is used regardless of Re .

For the case of $Re = 50$, the bubble reaches a deformed stable state. As observed in previous sections, when the value of Re is slightly below the critical Re condition, the bubble does not settle into a deformed stable state but instead alternates in an elongation and contraction process. In comparison to the $Re = 50$ case on the left, the right image in Fig. 8 ($Re = 93$) shows a higher shear stress profile near the bubble endpoints as it undergoes an elongation state in the process toward breakup. The value of the maximum shear stress for the case of $Re = 50$ is $\tau^* \approx 6$ and the maximum shear stress for the case of $Re = 93$ at the moment shown in Fig. 8 has the value of $\tau^* \approx 8$. The shear stress profile in Fig. 8 (color contour) is drawn in the range from $\tau^* = 1$ to $\tau^* = 8$, but, for emphasis, shear stress regions with $\tau^* \geq 6$ are illustrated in red. As can be seen in the figure, the strongest shear stresses are concentrated on the ends of the bubble for both Re conditions. This indicates that the strong shear stresses acting on the ends of the bubble are responsible for much of the

451 bubble stretching. It is important to note that the magnitude of the shear stress
452 acting on the ends of the bubble for the case of $Re = 93$ is much larger than
453 that for the case of $Re = 50$.

454 We also observe that the shear stress *inside* the bubble was very small relative
455 to that of the matrix fluid due to very small density and viscosity of the bubble.
456 Since the force of strong shear stresses acting on the ends of the bubble is
457 difficult to transfer across the interface, as a consequence, a sufficiently large Re
458 condition is required for large bubble deformations.

459 In summary, what we discover is that for the Reynolds number sufficiently below
460 the critical value, a relatively quick unsteady elongation period gives way to a
461 steady state (with no break up). On the other hand for Reynolds number *close*
462 to the critical Reynolds number, there is a prolonged, unsteady, elongation
463 period, in which periodic motion is observed and the deformation parameter
464 D is close to one. The “vacillating” behavior cannot last forever, ultimately
465 (perhaps stochastically!), the bubble will either settle down or break. We assert
466 that regardless of the outcome, this vacillating behaviour will always occur in
467 close proximity to the critical Reynolds’ number. In other words, regardless of
468 the outcome, we claim, using the grid resolution of $R/16$, that one is assured
469 of being within 3 percent of the critical Reynolds number (see Figure 3). In
470 fact, we hypothesize that there will *always* be “vacillating” behavior if one is
471 sufficiently close to the critical Reynolds number. i.e. given an almost infinite
472 supply of computational resources, as one hones in closer and closer to the
473 critical Reynolds number, a “tug of war” will be observed between the surface
474 tension force trying to pull the bubble together versus the wall driven shear
475 stress trying to pull the bubble apart.

476 *4.4. Velocity field outside and inside the breaking bubble*

477 In this section, we consider the fluid flow velocity field outside and inside the
478 bubble during the shear-induced breakup process. Figure 9 shows the velocity
479 fields outside and inside the bubble at cross-sectional slices in the xz -plane
480 for a flow condition of $Ca = 0.3$ and $Re = 93$. Regions around the bubble
481 where there is a higher density of velocity vectors correspond to the level-1 grid
482 portion of the AMR structure. The simulation results show that the velocity
483 field inside the bubble is particularly distinct from the surrounding flow field
484 in the exterior of the bubble. The cross-sections at $T = 12.2$ and $T = 18.1$,
485 taken during the elongation phase, show how shear forces at the lower and
486 upper halves of the bubble act along the bottom and top surfaces, respectively,
487 to deform the interface. Near the left and right edges of the bubble, inward
488 interior flows (that point toward the bubble center) begin to develop. Strong
489 shearing forces in the exterior near the bottom-left-end and top-right-end of
490 the bubble interact with the interior flow field through the boundary to create
491 cusped shapes at the bottom-left and top-right ends of the bubble while the
492 interface is laterally elongated in the x -direction. During the shrinking process,
493 which occurs for $23.6 \leq T \leq 27.8$, inward flows within the bubble extend over
494 a wider region and are no longer localized near the bubble edges. Then, we
495 observe that circulating flows form at the thread-bridge part of the doglegged

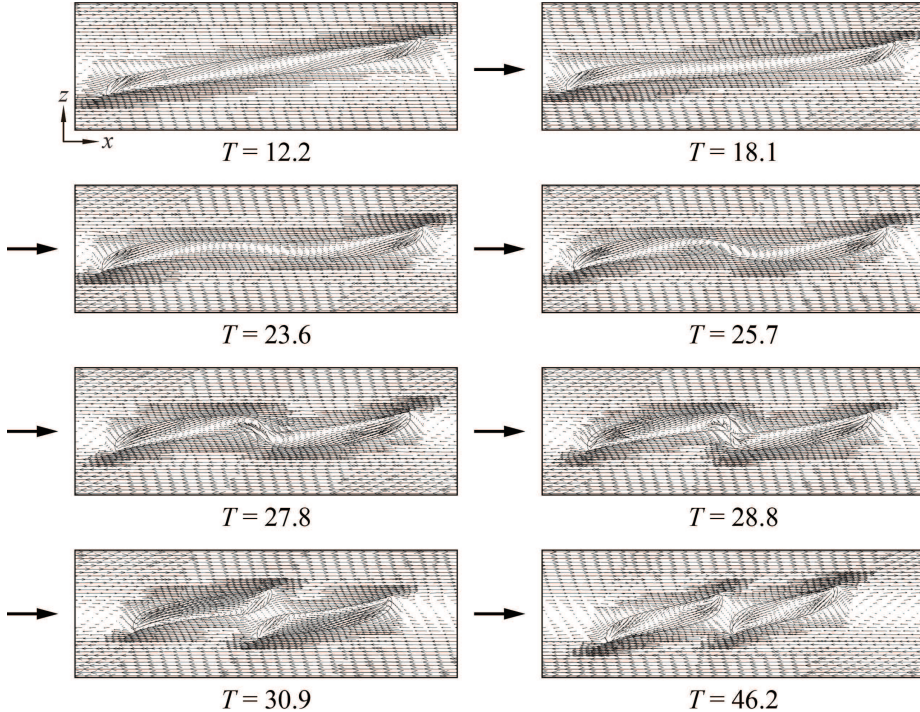


Figure 9: Fluid velocity field outside and inside the breaking bubble in shear flow at the condition $Ca = 0.3$ and $Re = 93$. The “bubble” critical Reynolds number corresponding to $Ca = 0.3$ is $92 < Re_c < 93$. ($\lambda = 1.2 \times 10^{-3}$, $\eta < 1.0 \times 10^{-3}$)

496 bubble shape over the time interval [25.7, 27.8]. During the breakup process
 497 (T \sim 28.8), higher-intensity inward flows are formed inside the bubble, near the
 498 pinch off region, that are naturally larger than the surrounding interior flows
 499 and which are inextricably associated with the bubble migration illustrated in
 500 Figs. 6 and 7. As time proceeds further (T = 46.2), distinct inward flows are
 501 formed inside the daughter bubbles; the bubbles then begin their migration
 502 toward the side walls. Considering the left daughter bubble, for example, we
 503 see that the mechanism responsible for this movement results from larger shear
 504 forces acting on the bottom-left end than those in the top-left end.

505 *4.5. Effect of surface tension on bubble deformation and breakup*

506 In previous sections, we considered numerical simulations of bubble deforma-
 507 tion and breakup with a capillary number $Ca = 0.3$. Here, we examine
 508 similar bubble dynamics with $Ca = 0.8$ and we also investigate the effect of in-
 509 terfacial tension on bubble deformation and breakup. Using $Ca = 0.8$ for both
 510 cases, Figures 10 and 11 present the time evolution of shear-induced bubble
 511 deformation and breakup with $Re = 42$ and $Re = 43$, respectively. We note
 512 that the bubble critical Reynolds number is around $Re_c \approx 43$, whereas $Re_c \approx 0$

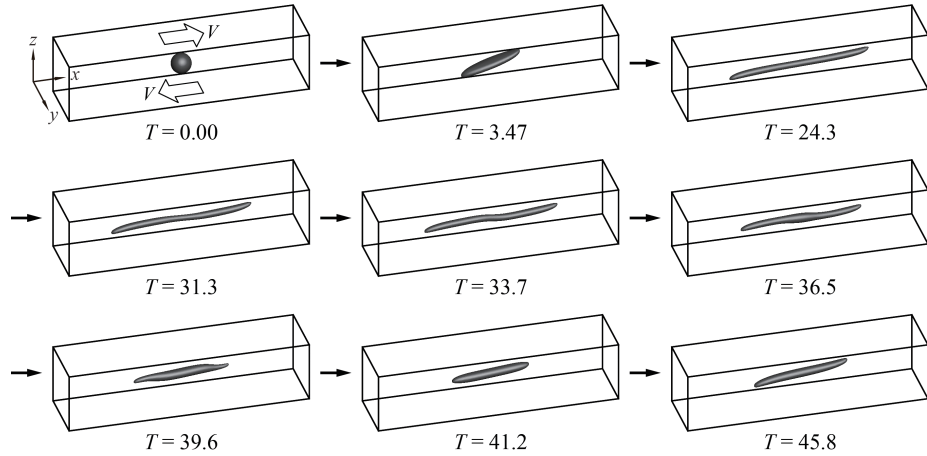


Figure 10: Time evolution of bubble deformation in shear flow at the condition of $Ca = 0.8$ and $Re = 42$. The “bubble” critical Reynolds number corresponding to $Ca = 0.8$ is $42 < Re_c < 43$. ($\lambda = 1.2 \times 10^{-3}$, $\eta < 1.0 \times 10^{-3}$)

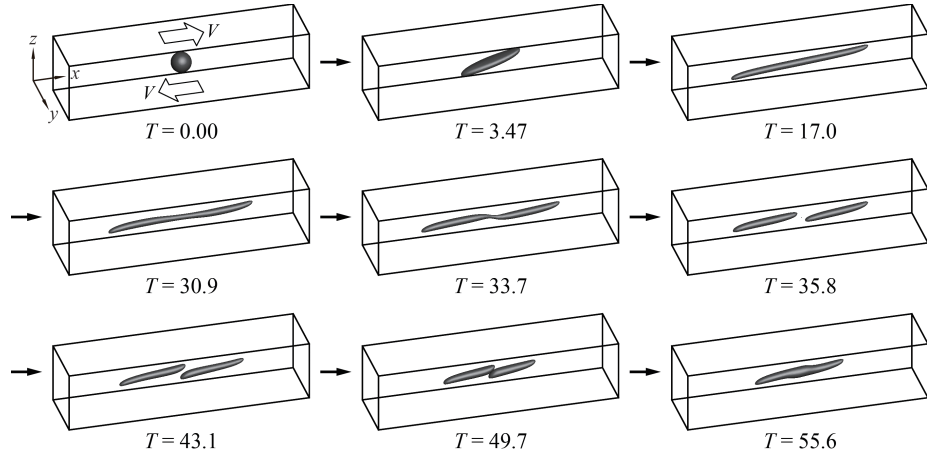


Figure 11: Time evolution of bubble deformation in shear flow at the condition of $Ca = 0.8$ and $Re = 43$. The “bubble” critical Reynolds number corresponding to $Ca = 0.8$ is $42 < Re_c < 43$. ($\lambda = 1.2 \times 10^{-3}$, $\eta < 1.0 \times 10^{-3}$)

513 for the corresponding case of the drop with $\lambda = \eta = 1$ (see e.g. Li et al. [22]).
 514 Note that Re_c for $Ca = 0.8$ is smaller than that for the condition of $Ca = 0.3$
 515 since the bubble at $Ca = 0.8$ is more elastic due to the weaker effect of sur-
 516 face tension in this case. The results shown in Figs. 10 and 11 indicate that
 517 the bubble deformation and breakup process for the condition of $Ca = 0.8$ is
 518 analogous to that for $Ca = 0.3$. For the case of bubble deformation without
 519 breakup (Fig. 10), the bubble initially assumes a long elongated shape along the
 520 x -direction at around $T = 24.3$. The bubble then enters a compression stage
 521 over the time interval $[31.3, 41.2]$ and subsequently starts to elongate again at
 522 $T = 45.8$. On the other hand, for the case of bubble breakup (Fig. 11), an
 523 initial elongation phase is followed by a doglegged shape formation at $T = 33.7$.
 524 After that, the bubble ruptures from the thread-bridge part of the doglegged
 525 shape and two daughter bubbles are produced ($T = 35.8$). The two daughter
 526 bubbles formed after breakup move to the central area ($T = 49.7$) as in the case
 527 of $Ca = 0.8$ and $Re = 93$, but the two bubbles eventually coalesce in a region
 528 approximately centered in the computational domain ($T = 55.6$). We note that
 529 in a real experimental setting, bubbles may coalesce after breaking up due to
 530 slight deviations of flow conditions and states. Although the process of bubble
 531 deformation and breakup for flow conditions with $Ca = 0.3$ and $Ca = 0.8$ are
 532 similar, a pronounced difference is that the bubble for $Ca = 0.8$ is more elon-
 533 gated and slender than that for $Ca = 0.3$ due to the smaller effect of surface
 534 tension for $Ca = 0.8$.

535 Table 4 lists, for representative Ca values, the corresponding critical Reynolds
 536 number, Re_c , for shear-induced bubble breakup. The data in Table 4 corre-
 537 sponds to $\lambda = 1.2 \times 10^{-3}$, $\eta < 1.0 \times 10^{-3}$, $0.3 < Ca < 1$, and the initial/boundary
 538 conditions are given by (1). The results in Table 4 indicate that sufficiently large
 539 shear forces are required for bubble breakup even for large capillary numbers.
 540 In Figure 12 we plot the smooth interpolant of the data given in Table 4 and
 541 make the hypothesis that given a new data point, (Ca, Re) , shear induced bub-
 542 ble break up will occur if the point (Ca, Re) is above the given critical curve,
 543 and the bubble will not break if the (Ca, Re) pair is below the critical curve.
 544 For comparison, a critical curve for the drop with $\lambda = \eta = 1$ is also indicated
 545 in Fig. 12. The inclusion of breakup and no-breakup critical curves, for both
 546 the drop and the bubble, will facilitate future identification of Re_c numbers—
 547 and thus a more complete general critical curve—for a wide range of high Ca
 548 numbers.

Table 4: Shear-induced bubble breakup for various flow conditions described in terms of column pairs of critical Reynolds numbers and corresponding capillary numbers. ($\lambda = 1.2 \times 10^{-3}$, $\eta < 1.0 \times 10^{-3}$)

| Capillary number Ca | 0.3 | 0.5 | 0.8 | 1.0 |
|---------------------------------|-----|-----|-----|-----|
| Critical Reynolds number Re_c | 93 | 67 | 43 | 35 |

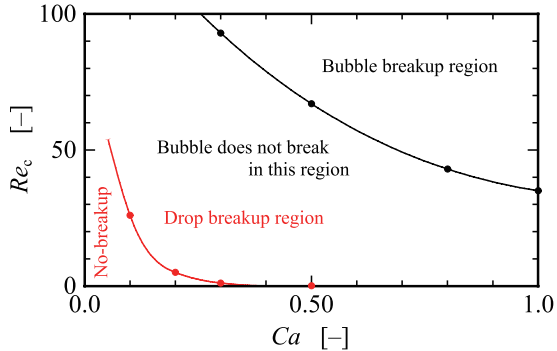


Figure 12: A plot of the critical Reynolds number versus capillary number for the data listed in Table 4. $\lambda = 1.2 \times 10^{-3}$, $\eta < 1.0 \times 10^{-3}$, $0.3 < Ca < 1$, and the initial/boundary conditions are given by (1). Given a new data point, (Ca, Re) , one can reliably predict whether the given (Ca, Re) pair will result in shear induced bubble break-up or not. Note, for the “Drop delineation curve,” $\lambda = \eta = 1$.

549 5. Conclusions

550 The bubble deformation and breakup process in simple linear shear flow
 551 liquid was explored numerically using the CLSVOF computational method. In
 552 this study, the critical Reynolds number Re_c , at which bubble breakup first
 553 occurs, was determined for several flow conditions, and the differences between
 554 bubble deformation and breakup were compared with the well-known analogous
 555 process of drop deformation and breakup.

556 Numerical results revealed significant differences between bubble deforma-
 557 tion and breakup and the corresponding drop dynamics. For case of bubble,
 558 it was discovered that much stronger shear flows are necessary to induce in-
 559 terface breakup compared with a drop immersed in a similar flow field. That
 560 is, a much larger Reynolds number flow is required in order to induce bubble
 561 breakup. The behavior of bubble breakup was very similar through the Ca
 562 number range considered in our computations: the bubble underwent a sim-
 563 ilar breakup mechanism in which rupture occurred at a thread-bridge part that
 564 followed a doglegged shape formation stage. In bubble deformation without
 565 breakup, near Re_c , the bubble did not maintain a stable deformed shape, in
 566 contrast to drop deformation near the critical Reynolds number. The bubble
 567 exhibited pronounced underdamped behavior: the bubble oscillated between
 568 elongating and shrinking motions for non-rupturing flow conditions.

569 We attribute the large differences in morphology for the bubble undergo-
 570 ing breakup, compared with the drop, to the density and viscosity ratio. The
 571 density and viscosity ratio remarkably impacts on bubble/drop deformation
 572 and breakup. The bubble deformation and breakup is subject to a synergistic
 573 coupling of the density and viscosity ratio, and whose effect will be examined
 574 separately in future work.

575 **References**

- 576 [1] Amani, A., Balcázar, N., Castro, J., Oliva, A., 2019. Numerical study of droplet deformation in shear flow using a conservative level-set method. *Chemical Engineering Science* 207,
577 153–171. URL: <http://www.sciencedirect.com/science/article/pii/S0009250919305123>, doi:<https://doi.org/10.1016/j.ces.2019.06.014>.
- 582 [2] Bazhlekov, I.B., Anderson, P.D., Meijer, H.E., 2006. Numerical investigation of the effect of insoluble surfactants on drop deformation and
583 breakup in simple shear flow. *Journal of Colloid and Interface Science* 298, 369 – 394. URL: <http://www.sciencedirect.com/science/article/pii/S0021979705012658>, doi:<http://dx.doi.org/10.1016/j.jcis.2005.12.017>.
- 588 [3] Bento, D., Rodrigues, R.O., Faustino, V., Pinho, D., Fernandes, C.S.,
589 Pereira, A.I., Garcia, V., Miranda, J.M., Lima, R., 2018. Deformation
590 of red blood cells, air bubbles, and droplets in microfluidic devices:
591 Flow visualizations and measurements. *Micromachines* 9, 151. URL:
592 <https://www.mdpi.com/2072-666X/9/4/151>, doi:10.3390/mi9040151.
- 593 [4] Chu, P., Finch, J., Bournival, G., Ata, S., Hamlett, C., Pugh, R.J.,
594 2019. A review of bubble break-up. *Advances in Colloid and Interface
595 Science* 270, 108–122. URL: <https://www.sciencedirect.com/science/article/pii/S0001868619300211>, doi:<https://doi.org/10.1016/j.cis.2019.05.010>.
- 598 [5] Cristini, V., Bławzdziewicz, J., Loewenberg, M., 2001. An adaptive
599 mesh algorithm for evolving surfaces: simulations of drop breakup
600 and coalescence. *Journal of Computational Physics* 168, 445 –
601 463. URL: <http://www.sciencedirect.com/science/article/pii/S0021999101967130>, doi:<http://dx.doi.org/10.1006/jcph.2001.6713>.
- 603 [6] Cristini, V., Guido, S., Alfani, A., Bławzdziewicz, J., Loewenberg, M.,
604 2003. Drop breakup and fragment size distribution in shear flow. *Journal
605 of Rheology* 47, 1283–1298. URL: <http://scitation.aip.org/content/sor/journal/jor2/47/5/10.1122/1.1603240>, doi:<http://dx.doi.org/10.1122/1.1603240>.
- 608 [7] Croce, R., Griebel, M., Schweitzer, M.A., 2010. Numerical simulation of
609 bubble and droplet deformation by a level set approach with surface tension
610 in three dimensions. *International Journal for Numerical Methods in Fluids*
611 62, 963–993. URL: <http://dx.doi.org/10.1002/fld.2051>, doi:10.1002/fld.2051.
- 613 [8] Drenckhan, W., Saint-Jalmes, A., 2015. The science of foaming. *Advances
614 in Colloid and Interface Science* 222, 228–259. URL: <https://doi.org/10.1016/j.jcis.2015.06.001>.

- 615 [//www.sciencedirect.com/science/article/pii/S0001868615000603](http://www.sciencedirect.com/science/article/pii/S0001868615000603),
 616 doi:<https://doi.org/10.1016/j.cis.2015.04.001>. reinhard Miller,
 617 Honorary Issue.
- 618 [9] Ervin, E., Tryggvason, G., 1997. The rise of bubbles in a vertical shear
 619 flow. *Journal of Fluids Engineering* 119(2), 443–449.
- 620 [10] Hernandez, F.H., Rangel, R.H., 2017. Breakup of drops in simple
 621 shear flows with high-confinement geometry. *Computers & Fluids* 146,
 622 23 – 41. URL: <http://www.sciencedirect.com/science/article/pii/S0045793017300038>, doi:<https://doi.org/10.1016/j.compfluid.2017.01.001>.
- 625 [11] Hirt, C., Nichols, B., 1981. Volume of fluid (vof) method
 626 for the dynamics of free boundaries. *Journal of Computational
 627 Physics* 39, 201 – 225. URL: <http://www.sciencedirect.com/science/article/pii/0021999181901455>, doi:[http://dx.doi.org/10.1016/0021-9991\(81\)90145-5](http://dx.doi.org/10.1016/0021-9991(81)90145-5).
- 630 [12] Inamuro, T., 2006. Lattice boltzmann methods for viscous fluid flows and
 631 for two-phase fluid flows. *Fluid Dynamics Research* 38, 641. URL: <http://stacks.iop.org/1873-7005/38/i=9/a=A04>.
- 633 [13] Inamuro, T., Tomita, R., Ogino, F., 2003. Lattice boltzmann simu-
 634 lations of drop deformation and breakup in simple shear flows. *Inter-
 635 national Journal of Modern Physics B* 17, 21–26. URL: <http://www.worldscientific.com/doi/abs/10.1142/S0217979203017035>, doi:[10.1142/S0217979203017035](https://doi.org/10.1142/S0217979203017035).
- 638 [14] Ioannou, N., Liu, H., Zhang, Y., 2016. Droplet dynamics
 639 in confinement. *Journal of Computational Science* 17, 463 –
 640 474. URL: <http://www.sciencedirect.com/science/article/pii/S1877750316300308>, doi:<https://doi.org/10.1016/j.jocs.2016.03.009>. discrete Simulation of Fluid Dynamics 2015.
- 643 [15] Janssen, P., Anderson, P., 2008. A boundary-integral model for
 644 drop deformation between two parallel plates with non-unit viscosity
 645 ratio drops. *Journal of Computational Physics* 227, 8807–
 646 8819. URL: <http://www.sciencedirect.com/science/article/pii/S002199910800346X>, doi:<http://dx.doi.org/10.1016/j.jcp.2008.06.027>.
- 649 [16] Janssen, P.J.A., Anderson, P.D., 2007. Boundary-integral method
 650 for drop deformation between parallel plates. *Physics of Fluids*
 651 19. URL: <http://scitation.aip.org/content/aip/journal/pof2/19/4/10.1063/1.2715621>, doi:<http://dx.doi.org/10.1063/1.2715621>.
- 653 [17] Kang, M., Fedkiw, R.P., Liu, X.D., 2000. A boundary condition capturing
 654 method for multiphase incompressible flow. *Journal of scientific computing*
 655 15, 323–360.

- 656 [18] Khismatullin, D.B., Renardy, Y., Cristini, V., 2003. Inertia-induced
 657 breakup of highly viscous drops subjected to simple shear. Physics of Fluids
 658 15, 1351–1354. doi:<http://dx.doi.org/10.1063/1.1564825>".
- 659 [19] Komrakova, A., Shardt, O., Eskin, D., Derksen, J., 2014. Lattice
 660 boltzmann simulations of drop deformation and breakup in shear flow.
 661 International Journal of Multiphase Flow 59, 24 – 43. URL: <http://www.sciencedirect.com/science/article/pii/S0301932213001547>,
 662 doi:<http://dx.doi.org/10.1016/j.ijmultiphaseflow.2013.10.009>.
- 663 [20] Komrakova, A., Shardt, O., Eskin, D., Derksen, J., 2015. Effects
 664 of dispersed phase viscosity on drop deformation and breakup
 665 in inertial shear flow. Chemical Engineering Science 126, 150 –
 666 159. URL: <http://www.sciencedirect.com/science/article/pii/S000925091400726X>, doi:<http://dx.doi.org/10.1016/j.ces.2014.12.012>.
- 667 [21] Legendre, D., Magnaudet, J., 1998. The lift force on a spherical bubble in
 668 a viscous linear shear flow. Journal of Fluid Mechanics 368, 81–126.
- 669 [22] Li, J., Renardy, Y., Renardy, M., 2000. Numerical simulation of
 670 breakup of a viscous drop in simple shear flow through a volume-of-fluid
 671 method. Physics of Fluids 12, 269–282. URL: <http://scitation.aip.org/content/aip/journal/pof2/12/2/10.1063/1.870305>, doi:<http://dx.doi.org/10.1063/1.870305>.
- 671 [23] Müller-Fischer, N., Tobler, P., Dressler, M., Fischer, P., Windhab, E.J.,
 672 2008. Single bubble deformation and breakup in simple shear flow. Experiments
 673 in fluids 45, 917–926.
- 674 [24] Ohta, M., Kikuchi, D., Yoshida, Y., Sussman, M., 2011. Robust numerical
 675 analysis of the dynamic bubble formation process in a viscous liquid.
 676 International Journal of Multiphase Flow 37, 1059–1071.
- 677 [25] Rallison, J.M., 1984. The deformation of small viscous drops
 678 and bubbles in shear flows. Annual Review of Fluid Mechanics 16, 45–66. URL: <http://dx.doi.org/10.1146/annurev.fl.16.010184.000401>,
 679 doi:[http://dx.doi.org/10.1146/annurev.fl.16.010184.000401">http://dx.doi.org/10.1146/annurev.fl.16.010184.000401](http://dx.doi.org/10.1146/annurev.fl.16.010184.000401).
- 680 [26] Renardy, Y., 2006. Numerical simulation of a drop undergoing large am-
 681 plitude oscillatory shear. Rheologica acta 45, 223–227.
- 682 [27] Renardy, Y., 2007. The effects of confinement and inertia on the production
 683 of droplets. Rheologica Acta 46, 521–529. URL: <http://dx.doi.org/10.1007/s00397-006-0150-y>, doi:[10.1007/s00397-006-0150-y](http://dx.doi.org/10.1007/s00397-006-0150-y).
- 684 [28] Renardy, Y., 2008. Effect of startup conditions on drop breakup
 685 under shear with inertia. International Journal of Multiphase Flow

- 695 34, 1185 – 1189. URL: <http://www.sciencedirect.com/science/article/pii/S030193220800089X>, doi:<http://dx.doi.org/10.1016/j.ijmultiphaseflow.2008.04.004>.
- 696
- 697
- 698 [29] Renardy, Y., Cristini, V., 2001a. Effect of inertia on drop breakup under
699 shear. Physics of Fluids 13, 7–13. URL: <http://scitation.aip.org/content/aip/journal/pof2/13/1/10.1063/1.1331321>, doi:<http://dx.doi.org/10.1063/1.1331321>.
- 700
- 701
- 702 [30] Renardy, Y., Cristini, V., Li, J., 2002. Drop fragment distributions under
703 shear with inertia. International Journal of Multiphase Flow 28, 1125
704 – 1147. URL: <http://www.sciencedirect.com/science/article/pii/S0301932202000228>, doi:[http://dx.doi.org/10.1063/S0301-9322\(02\)00022-8](http://dx.doi.org/10.1063/S0301-9322(02)00022-8).
- 705
- 706
- 707 [31] Renardy, Y.Y., Cristini, V., 2001b. Scalings for fragments produced
708 from drop breakup in shear flow with inertia. Physics of Fluids 13,
709 2161–2164. URL: <https://doi.org/10.1063/1.1384469>, doi:[10.1063/1.1384469](https://doi.org/10.1063/1.1384469), arXiv:<https://doi.org/10.1063/1.1384469>.
- 710
- 711 [32] Rust, A., Manga, M., 2002. Bubble shapes and orientations in low re-
712 simple shear flow. Journal of Colloid and Interface Science 249, 476–
713 480. URL: <https://www.sciencedirect.com/science/article/pii/S0021979702982925>, doi:<https://doi.org/10.1006/jcis.2002.8292>.
- 714
- 715 [33] Stone, H.A., 1994. Dynamics of drop deformation and breakup
716 in viscous fluids. Annual Review of Fluid Mechanics 26,
717 65–102. URL: <http://dx.doi.org/10.1146/annurev.fl.26.010194.000433>,
718 doi:[10.1146/annurev.fl.26.010194.000433](https://doi.org/10.1146/annurev.fl.26.010194.000433),
719 arXiv:<http://dx.doi.org/10.1146/annurev.fl.26.010194.000433>.
- 720
- 721 [34] Sussman, M., 2003. A second order coupled level set and volume-
722 of-fluid method for computing growth and collapse of vapor bubbles.
723 Journal of Computational Physics 187, 110–136. URL: <https://www.sciencedirect.com/science/article/pii/S0021999103000871>,
724 doi:[https://doi.org/10.1016/S0021-9991\(03\)00087-1](https://doi.org/10.1016/S0021-9991(03)00087-1).
- 725
- 726 [35] Sussman, M., Almgren, A.S., Bell, J.B., Colella, P., Howell, L.H.,
727 Welcome, M.L., 1999. An adaptive level set approach for incom-
728 pressible two-phase flows. Journal of Computational Physics 148, 81
729 – 124. URL: <http://www.sciencedirect.com/science/article/pii/S002199919896106X>, doi:<https://doi.org/10.1006/jcph.1998.6106>.
- 730
- 731 [36] Sussman, M., Puckett, E.G., 2000. A coupled level set and
732 volume-of-fluid method for computing 3d and axisymmetric incompress-
733 ible two-phase flows. Journal of Computational Physics 162, 301–
734 337. URL: <http://www.sciencedirect.com/science/article/pii/S0021999100965379>, doi:<http://dx.doi.org/10.1006/jcph.2000.6537>.
- 735

- 735 [37] Sussman, M., Smereka, P., Osher, S., 1994. A level set ap-
 736 proach for computing solutions to incompressible two-phase flow.
 737 Journal of Computational Physics 114, 146 – 159. URL: <http://www.sciencedirect.com/science/article/pii/S0021999184711557>,
 738 doi:<http://dx.doi.org/10.1006/jcph.1994.1155>.
- 740 [38] Sussman, M., Smith, K., Hussaini, M., Ohta, M., Zhi-Wei, R., 2007. A
 741 sharp interface method for incompressible two-phase flows. Journal of Com-
 742 putational Physics 221, 469–505. URL: <https://www.sciencedirect.com/science/article/pii/S0021999106002981>, doi:<https://doi.org/10.1016/j.jcp.2006.06.020>.
- 745 [39] Tanguy, S., Ménard, T., Berlemont, A., 2007. A level set method for
 746 vaporizing two-phase flows. Journal of Computational Physics 221, 837–
 747 853.
- 748 [40] Taylor, G.I., 1932. The viscosity of a fluid containing small drops of another
 749 fluid. Proceedings of the Royal Society of London A: Mathematical, Phys-
 750 ical and Engineering Sciences 138, 41–48. doi:[10.1098/rspa.1932.0169](https://doi.org/10.1098/rspa.1932.0169).
- 751 [41] Taylor, G.I., 1934. The formation of emulsions in definable fields of flow.
 752 Proceedings of the Royal Society of London A: Mathematical, Physical and
 753 Engineering Sciences 146, 501–523. doi:[10.1098/rspa.1934.0169](https://doi.org/10.1098/rspa.1934.0169).
- 754 [42] Unverdi, S.O., Tryggvason, G., 1992. A front-tracking method
 755 for viscous, incompressible, multi-fluid flows. Journal of Computa-
 756 tional Physics 100, 25 – 37. URL: <http://www.sciencedirect.com/science/article/pii/002199919290307K>, doi:[http://dx.doi.org/10.1016/0021-9991\(92\)90307-K](http://dx.doi.org/10.1016/0021-9991(92)90307-K).
- 759 [43] Wang, Z., Shi, D., Zhang, A., 2015. Three-dimensional lattice boltz-
 760 mann simulation of bubble behavior in a flap-induced shear flow. Com-
 761 puters & Fluids 123, 44 – 53. URL: <http://www.sciencedirect.com/science/article/pii/S0045793015003199>, doi:<https://doi.org/10.1016/j.compfluid.2015.09.007>.
- 764 [44] Wei, Y.K., Qian, Y., Xu, H., 2012. Lattice boltzmann simulations
 765 of single bubble deformation and breakup in a shear flow. The Jour-
 766 nal of Computational Multiphase Flows 4, 111–117. URL: <https://doi.org/10.1260/1757-482X.4.1.111>, doi:[10.1260/1757-482X.4.1.111](https://doi.org/10.1260/1757-482X.4.1.111), arXiv:<https://doi.org/10.1260/1757-482X.4.1.111>.
- 769 [45] Zhang, J., Miksis, M.J., Bankoff, S.G., 2006. Nonlinear dynamics of
 770 a two-dimensional viscous drop under shear flow. Physics of Fluids
 771 18. URL: <http://scitation.aip.org/content/aip/journal/pof2/18/7/10.1063/1.2222336>, doi:<http://dx.doi.org/10.1063/1.2222336>.
- 773 [46] Zhang, J., Ni, M.J., Magnaudet, J., 2021a. Three-dimensional dynamics
 774 of a pair of deformable bubbles rising initially in line. part 1. moderately
 775 inertial regimes. Journal of Fluid Mechanics 920, A16.

- 776 [47] Zhang, J., Ni, M.J., Magnaudet, J., 2022. Three-dimensional dynamics of
777 a pair of deformable bubbles rising initially in line. part 2. highly inertial
778 regimes. Journal of Fluid Mechanics 943, A10.
- 779 [48] Zhang, J., Shu, S., Guan, X., Yang, N., 2021b. Regime map-
780 ping of multiple breakup of droplets in shear flow by phase-field
781 lattice boltzmann simulation. Chemical Engineering Science 240,
782 116673. URL: <https://www.sciencedirect.com/science/article/pii/S0009250921002384>, doi:<https://doi.org/10.1016/j.ces.2021.116673>.
783
784